

# Altermagnetic Even-Odd Effects in $\text{CsV}_2\text{Te}_2\text{O}$ Josephson Junctions

Chuang Li,<sup>1,\*</sup> Jin-Xing Hou,<sup>2,3,\*</sup> Shuai-Ling Zhu,<sup>1</sup> Hao Zheng,<sup>1</sup>  
Yu Song,<sup>1</sup> Yang Liu,<sup>1</sup> Song-Bo Zhang,<sup>2,3,†</sup> and Lun-Hui Hu<sup>1,‡</sup>

<sup>1</sup>*Center for Correlated Matter and School of Physics, Zhejiang University, Hangzhou 310058, China*

<sup>2</sup>*Hefei National Laboratory, Hefei, Anhui, 230088, China*

<sup>3</sup>*International Center for Quantum Design of Functional Materials (ICQD),  
University of Science and Technology of China, Hefei, Anhui 230026, China*

The interplay between conventional superconductivity and unconventional magnetism offers an exciting platform for realizing exotic superconducting phenomena. Here, we investigate Josephson effects in planar and vertical junctions based on  $\text{CsV}_2\text{Te}_2\text{O}$ -family materials, which host hidden *d*-wave altermagnetism with G-type antiferromagnetic order. In monolayer-based planar junctions, the quasi-1D, nearly flat, spin-polarized bands of the altermagnet, when coupled to *s*-wave superconductors, produce a *fully* spin-polarized supercurrent with strong directional anisotropy—a spin-selective Josephson effect. In multilayers, we uncover an *altermagnetic even-odd effect*: spin-polarized supercurrents persist only in odd-layer planar junctions but cancel exactly in even layers. Thus, layer parity acts as a switch for spin-polarized supercurrent. In vertical junctions, odd-layer barriers enhance equal-spin triplet transport while even layers favor opposite-spin transport, yielding a robust period-two oscillation in the total supercurrent with layer number. These layer-parity-dependent responses represent a general even-odd effect in hidden altermagnets, applicable to diverse magnetic and transport phenomena.

## Introduction

Unconventional magnetism has emerged as a cornerstone of condensed matter physics [1–11]. A pivotal development in this field is the recent identification of collinear altermagnetism [12–21], which has since spurred intense theoretical interest [22–44] and triggered numerous experimental investigations [45–61]. Unlike conventional Néel antiferromagnets, altermagnets are characterized by a compensated magnetic order that hosts momentum-dependent spin polarization, opening a distinct route to spin-control without net magnetization [62–66]. This novel phase has recently been realized in the van der Waals  $\text{CsV}_2\text{Te}_2\text{O}$  family, identified as a *d*-wave altermagnet in the 2D limit [67–77]. In these systems, the Lieb lattice formed by the  $\text{V}_2\text{O}$  planes gives rise to quasi-1D spin-polarized flat bands and spin-valley locking Fermi surfaces [18], which can in turn give rise to unconventional electromagnetic responses and spin-dependent transport phenomena [78–82].

Despite its layered, device-friendly structure, the  $\text{CsV}_2\text{Te}_2\text{O}$  family poses a fundamental constraint for spin-dependent applications: it is a G-type antiferromagnet in the bulk [72, 73], which preserves the combined inversion-time-reversal symmetry and therefore guarantees spin-degenerate bulk bands. Nonetheless, the weak inter-layer coupling allows each layer to retain its local altermagnetic character [73]. This gives rise to layer-resolved altermagnetic spin-split bands—a phase recently termed hidden altermagnetism or anti-altermagnetism—which can still host novel spin-dependent phenomena [83–85]. It remains an open question whether hidden altermagnet-based junctions can host superconducting phenomena with no analogue in other magnetic systems.

In this work, we demonstrate that the hidden altermagnetism in the  $\text{CsV}_2\text{Te}_2\text{O}$  family [73] leads to pronounced altermagnetic even-odd effects in both planar and vertical Josephson junctions with Rashba superconductors. In planar junctions with odd-layer systems, the quasi-1D spin-polarized bands couple selectively to superconducting leads, producing a spin-selective Josephson effect in which the critical supercurrent is fully spin-polarized and exhibits strong directional anisotropy. In contrast, even-layer structures exhibit complete cancellation of spin-polarized supercurrents between top and bottom layers, suppressing this spin-selectivity. In vertical junctions, odd-layer barriers promote equal-spin triplet transport and suppress the opposite-spin contribution, while even-layer barriers do the converse. Accordingly, the supercurrent alternates between larger and smaller values every added layer, producing a period-two modulation atop an overall decay with increasing barrier thickness. Our results establish hidden altermagnets as a unique platform for achieving gate-tunable, spin-polarized supercurrents without net magnetization, opening a new route toward superconducting spintronic devices.

## Material and Effective Model

We focus on  $\text{CsV}_2\text{Te}_2\text{O}$  as our model system. Substitutions such as Rb or K for Cs do not introduce charge doping, and will not alter our main conclusions. The crystal structure belongs to the space group  $P4/mmm$  (point group  $D_{4h}$ ), with generators given by the four-fold rotation  $C_{4z}$ , the two-fold rotation  $C_{2x}$ , and the out-of-plane reflection  $M_z$ . As illustrated in Fig. 1(a), the  $\text{V}_2\text{O}$  planes form a Lieb lattice and support two competing magnetic orders. In both, the two V sublattices exhibit opposite spin polarization within the layer, an arrangement that can be interchanged only through ro-

tation or reflection—the defining characteristic of altermagnetism [18]. The orders differ in their inter-layer coupling: the C-type phase is ferromagnetic between layers [left panel in Fig. 1(a)], whereas the G-type phase is anti-ferromagnetically stacked [right panel in Fig. 1(a)]. By symmetry, the C-type phase is a bulk altermagnet, while the G-type phase—in which neighboring layers host opposite altermagnetic spin-splitting—corresponds to a hidden altermagnet [73].

$\text{CsV}_2\text{Te}_2\text{O}$  is a quasi-2D material with weak inter-layer coupling. We calculate its band structure using a monolayer model. The nonmagnetic band structure without spin-orbit coupling is shown in Fig. 1(b). The electronic states near the Fermi level are dominated by the  $3d$  orbitals of V atoms and are primarily shaped by the crystal field from the surrounding oxygen atoms. As revealed by quasi-particle interference measurements from scanning tunneling microscopy [74–76], the low-energy electronic structure is characterized by quasi-1D flat bands. Our orbital-resolved calculations in Fig. 1(c), plotted along the high-symmetry line, demonstrate that these experimentally observed bands derive primarily from the  $d_{xz}$  and  $d_{yz}$  orbitals [86]. Although the dispersion is not perfectly flat, the Fermi momentum lies near  $\pi/2$ , where  $\cos k_x \approx 0$  or  $\cos k_y \approx 0$ , resulting in quasi-1D Fermi surfaces with flat segments. Guided by this experimental and theoretical fingerprint, we construct the effective model based on these two dominant orbitals [87].

The crystal field further simplifies the model. Originating from the two oxygen atoms bonded to each V site along the bond direction, the local field significantly lifts the orbital degeneracy [68]. This results in an on-site energy splitting  $\Delta_{\text{CF}} = 1.24$  eV between the  $d_{xz}$  and  $d_{yz}$  orbitals [Fig. 1(c)]. Crucially, the sign of  $\Delta_{\text{CF}}$  changes between the two symmetry-inequivalent V atoms within the unit cell. Due to its sizable magnitude, this crystal-field configuration reduces the full Hilbert space  $[(A, B) \text{ sublattices} \otimes (d_{xz}, d_{yz}) \text{ orbitals}]$  to the low-energy subspace spanned by the states  $|A, d_{xz}\rangle$  and  $|B, d_{yz}\rangle$  [Fig. 1(d)]. Because of this sublattice-orbital locking, the sublattice index becomes redundant and will be omitted below. For the monolayer  $\text{CsV}_2\text{Te}_2\text{O}$ , the effective Hamiltonian in this two-band subspace reads,

$$\mathcal{H}_{\text{AM}}(\mathbf{k}) = [\epsilon_{2+}(\mathbf{k}) + \epsilon_3(\mathbf{k}) - \mu]\hat{\sigma}_0\hat{s}_0 + \epsilon_{2-}(\mathbf{k})\hat{\sigma}_z\hat{s}_0 + \epsilon_1(\mathbf{k})\hat{\sigma}_x\hat{s}_0 + M\hat{\sigma}_z\hat{s}_z, \quad (1)$$

where the basis is  $(d_{xz\uparrow}, d_{xz\downarrow}, d_{yz\uparrow}, d_{yz\downarrow})^T$  and  $\hat{\sigma}$  ( $\hat{s}$ ) are Pauli matrices for orbital (spin) degrees of freedom.  $\mathbf{k} = (k_x, k_y)$  denotes the momentum in the plane. The coefficients are  $\epsilon_{2\pm} = (t_\pi \pm t_\delta)(\cos k_x \pm \cos k_y)$ ,  $\epsilon_1 = -4t_1 \sin \frac{k_x}{2} \sin \frac{k_y}{2}$ , and  $\epsilon_3 = 4t_3 \cos k_x \cos k_y$ . Here,  $t_\pi$  and  $t_\delta$  denote the intra-sublattice hopping amplitudes from  $dd\pi$  and  $dd\delta$  bonds, respectively,  $t_1$  is the nearest neighbor inter-sublattice hopping, and  $t_3$  is a next-neighbor intra-sublattice hopping [all illustrated in

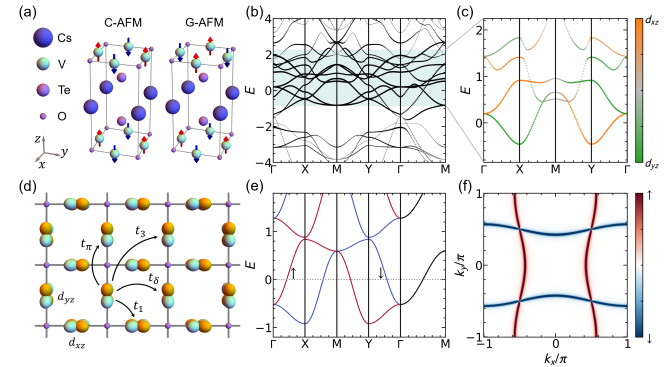


FIG. 1. Crystal and electronic structure of the  $d$ -wave altermagnetic  $\text{CsV}_2\text{Te}_2\text{O}$ . (a) Magnetic lattice structure showing C-type or G-type antiferromagnetic orders. (b) Nonmagnetic band structure of the monolayer; states near the Fermi level arise from V  $3d$  orbitals (light teal region). (c) Four-band projection near the Fermi level highlighting  $d_{xz}$  and  $d_{yz}$  orbitals. (d) The effective  $\text{V}_2\text{O}$  Lieb lattice model with orbital-sublattice locking. The hopping parameters are labeled with black arrows. (e)  $d$ -wave altermagnetic spin splitting bands from Eq. (1), with spins denoted by  $\uparrow$  and  $\downarrow$ . (f) Spin-resolved Fermi surface at the Fermi level [dashed line in (e)] featuring quasi-1D flat segments near  $k_x, k_y \approx \pm\pi/2$ .

Fig. 1(d)]. In addition,  $M$  and  $\mu$  denote the strength of the altermagnetic spin-splitting and the chemical potential, respectively. For  $M < 0$ , the magnetic splitting shifts the  $d_{xz,\downarrow}$  and  $d_{yz,\uparrow}$  orbitals away from the Fermi level, as shown in Fig. 1(e). This locking between atomic orbital and spin stems from the interplay between  $\Delta_{\text{CF}}$  and  $M$  [38, 39]. Moreover,  $M$  is on the order of 1 eV, allowing us to neglect the spin-orbit coupling.

In this work, we adopt the parameter set (in units of eV):  $t_\pi = -0.36$ ,  $t_\delta = 0.08$ ,  $t_1 = 0.03$ ,  $t_3 = 0.01$ ,  $M = -0.9$ ,  $\mu = -0.9$ , which can reproduce the experimentally observed quasi-particle interference patterns [76]. The monolayer system exhibits a  $d$ -wave altermagnetic phase [Figs. 1(e) and (f)], characterized by the spin-space symmetry generators:  $[U_s | C_{4z}] \triangleq i\hat{\sigma}_y\hat{s}_x$ ,  $[U_s | C_{2[110]}] \triangleq \hat{\sigma}_x\hat{s}_x$ . The altermagnetic nodal lines lie along the  $[110]$  and  $[\bar{1}\bar{1}0]$  directions. In multilayer structures with G-type antiferromagnetic order [72, 73], the additional symmetry  $[U_s | M_z] \triangleq \hat{\sigma}_0\hat{s}_x$  couples adjacent layers and enforces opposite altermagnetic spin-splitting between  $M_z$ -related layers, defining the hidden altermagnetic phase [83–85]. Consequently,  $[U_s | M_z]$  is naturally broken in thin films with an odd number of layers, providing a clear symmetry distinction between even- and odd-layer systems.

### Spin-selective Josephson effect

We begin by considering the monolayer  $\text{CsV}_2\text{Te}_2\text{O}$ , and investigate its superconducting proximity effect when coupled to a conventional  $s$ -wave superconductor with Rashba spin-orbit coupling. Such Rashba superconductors are widely observed in non-centrosymmetric materials [88]. The altermagnetic Fermi surface of  $\text{CsV}_2\text{Te}_2\text{O}$

consists of spin-polarized, nearly flat segments [Fig. 1(f)]. Consequently, transport along a principal crystal axis is facilitated by only one spin species [79]. In this work, we focus on Josephson junctions based on  $\text{CsV}_2\text{Te}_2\text{O}$ . When the junction is oriented along the  $x$  direction [Fig. 2(a)], the supercurrent is carried exclusively by spin- $\uparrow$  electrons, yielding a fully spin-polarized supercurrent. Strikingly, a simple  $90^\circ$  rotation of the junction to the  $y$  axis [Fig. 2(b)] completely reverses this polarization. We term this directional, fully polarized superconducting transport the *spin-selective Josephson effect*, a direct signature of the material's  $d$ -wave altermagnetic order.

To quantify the spin-selective Josephson effect, we employ the model in Eq. (1) to compute the supercurrent. For Rashba superconductor/altermagnet/Rashba superconductor junctions, we model the  $s$ -wave superconducting leads with  $C_{4z}$  symmetry,

$$\mathcal{H}_{\text{SC}}(\mathbf{k}) = \epsilon_s(\mathbf{k})\hat{\tau}_z\hat{s}_0 + \alpha(\sin k_x \hat{\tau}_z\hat{s}_y - \sin k_y \hat{\tau}_0\hat{s}_x) - \Delta(\cos \phi \hat{\tau}_y\hat{s}_y + \sin \phi \hat{\tau}_x\hat{s}_y), \quad (2)$$

where the Nambu basis is  $(c_{\mathbf{k},\uparrow}, c_{\mathbf{k},\downarrow}, c_{-\mathbf{k},\uparrow}^\dagger, c_{-\mathbf{k},\downarrow}^\dagger)^T$ , and  $\epsilon_s(\mathbf{k}) = -2t_s(\cos k_x + \cos k_y) - \mu_s$ . Here,  $t_s$ ,  $\mu_s$ ,  $\alpha$  are the hopping amplitude, chemical potential, and Rashba spin-orbit coupling strength, respectively;  $\Delta$  and  $\phi$  denote the  $s$ -wave pairing amplitude and the superconducting phase. We use parameters (in eV)  $t_s = 0.5$ ,  $\alpha = 0.4$ ,  $\mu_s = -0.5$  and  $\Delta = 0.02$ . This yields a superconducting coherence length of  $\xi_{\text{SC}} \approx 15$ . We confirm that our central results are robust and do not depend on this specific parameter set. Taking the junction along the  $x$ -direction as an example, the full Hamiltonian reads

$$H_{\text{JJ}}(x, k_y) = H_{\text{SC}1} + H_{\text{AM}} + H_{\text{SC}2} + H_{\text{coup}}, \quad (3)$$

where  $H_{\text{SC}1}$  and  $H_{\text{SC}2}$  describe the left and right superconducting leads (length  $L_{\text{SC}}$ ) with phases  $\phi_1$  and  $\phi_2$ , respectively, and  $H_{\text{AM}}$  is the central altermagnet of length  $L_{\text{AM}}$ . The term  $H_{\text{coup}}$  represents spin-independent hopping between the superconductors and the altermagnet. We assume translational invariance along  $y$ , while treating the  $x$ -direction with open boundaries and a finite number of layers. The explicit form of Eq. (3) is provided in the Methods section. Conservation of current allows the Josephson current to be calculated directly across the altermagnetic region [89–91],

$$I_{\text{tot}}^x(\phi_J) = -\frac{4e}{\hbar\beta} \sum_{k_y, \omega} \text{Im}[\text{Tr}[\hat{T}_h^\dagger \hat{F}(x+1) \hat{T}_e \hat{F}'(x)]], \quad (4)$$

where  $\phi_J = \phi_1 - \phi_2$  is the phase difference,  $\beta = 1/k_B T$ ,  $\omega = (2n+1)\pi/\beta$  are the fermionic Matsubara frequencies.  $\hat{T}_{e/h}(k_y)$  denote the electron (hole) hopping matrices, while  $\hat{F}(x, k_y, \omega)$  and  $\hat{F}'(x, k_y, \omega)$  represent the bulk and surface anomalous Green's functions at site  $x$ , respectively. These two matrices encode the proximity-induced

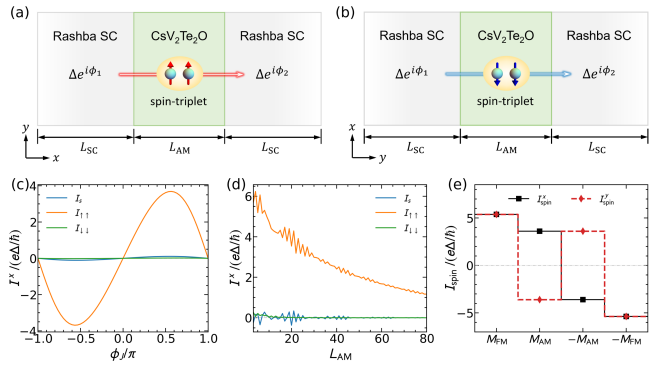


FIG. 2. Planar junctions in monolayer  $\text{CsV}_2\text{Te}_2\text{O}$ . (a) and (b) illustrate the spin-selective Josephson effect in  $s$ -wave superconductor/altermagnet/ $s$ -wave superconductor Josephson junctions. It is along the (a)  $x$  and (b)  $y$  directions. The proximity-induced pairing correlations in the altermagnet are anisotropic: (a) purely spin-up triplet; and (b) purely spin-down triplet. (c) For a short  $x$ -oriented junction ( $L_{\text{AM}} = 25$ ), the spin-singlet supercurrent  $I_s^x$  is significantly smaller than the spin-triplet supercurrent  $I_{\uparrow\uparrow}^x$ , while  $I_{\downarrow\downarrow}^x$  is vanishingly small. (d) Dependence of  $I_s^x$ ,  $I_{\uparrow\uparrow}^x$ , and  $I_{\downarrow\downarrow}^x$  on the junction length  $L_{\text{AM}}$ . (e) Comparison of the spin supercurrent for four different magnetic configurations: ferromagnetic order with  $\pm M_{\text{FM}}\hat{\sigma}_0\hat{s}_z$  and altermagnetic order with  $\pm M_{\text{AM}}\hat{\sigma}_z\hat{s}_z$ .

pair correlations within the altermagnet, directly linking them to the supercurrent via Eq. (4). In the spin basis,  $\hat{F}(x, k_y, \omega)$  decomposes into singlet and triplet components:  $\hat{F} = -i\hat{F}_s\hat{s}_y + \hat{F}_{\uparrow\uparrow}\frac{\hat{s}_0 + \hat{s}_z}{2} + \hat{F}_{\downarrow\downarrow}\frac{\hat{s}_0 - \hat{s}_z}{2} + \hat{F}_z\hat{s}_x$ , where  $\hat{F}_s$ ,  $\hat{F}_{\uparrow\uparrow}$ ,  $\hat{F}_{\downarrow\downarrow}$ , and  $\hat{F}_z$  are  $2 \times 2$  matrices in the orbital subspace, corresponding to spin-singlet, equal-spin-triplet, and opposite-spin-triplet correlations, respectively. Crucially, we find that only the  $\hat{F}_{\uparrow\uparrow}$  channel develops a non-zero proximity-induced pairing within the altermagnet, manifesting a fully spin-selective superconducting effect (see Methods). Consequently, the total Josephson current in Eq. (4) naturally separates into singlet, triplet, and mixed contributions,

$$I_{\text{tot}}^x(\phi_J) = I_s^x + I_z^x + I_{\uparrow\uparrow}^x + I_{\downarrow\downarrow}^x + I_{\text{mix}}^x. \quad (5)$$

Due to the spin U(1) symmetry of the altermagnet, the mixed term  $I_{\text{mix}}^x$  arises solely as a cross term between the spin-singlet and opposite-spin-triplet correlations. And it can only be activated via spin-orbit coupling within the altermagnet. The supercurrent for the  $y$ -oriented junction,  $I_{\text{tot}}^y(\phi_J)$ , is obtained analogously.

Figure 2(c) shows the current-phase relations for each component in a short  $x$ -direction junction ( $L_{\text{AM}} = 25$ ). Both the spin-singlet supercurrent  $I_s^x$  (blue curve) and the spin- $\uparrow$  polarized triplet supercurrent  $I_{\uparrow\uparrow}^x$  (orange curve) are present. As expected,  $I_s^x$  is significantly smaller than  $I_{\uparrow\uparrow}^x$ . Strikingly, despite the zero net magnetization of the altermagnet,  $I_{\uparrow\uparrow}^x$  dominates the transport, while  $I_{\downarrow\downarrow}^x$  (green curve) remains vanishingly small. This dominance originates from the nearly flat spin- $\downarrow$  Fermi

surface segment, whose vanishingly small Fermi velocity strongly suppresses its contribution to charge transport, leaving only the spin- $\uparrow$  band to carry the supercurrent. Moreover, the opposite-spin triplet term  $I_z^x$  is comparable in magnitude to  $I_s^x$ , while the mixing term  $I_{\text{mix}}^x$  vanishes identically (see Methods).

At a fixed  $\phi_J = \pi/2$ , we plot the supercurrent  $I_{s/\uparrow\uparrow/\downarrow\downarrow}^x$  versus junction length  $L_{\text{AM}}$  [Fig. 2(d)]. Both  $I_s^x$  and  $I_{\downarrow\downarrow}^x$  stay small and decay rapidly with distance, whereas the spin- $\uparrow$  channel persists. Hence, the Josephson supercurrent is fully spin-polarized over a wide range of junction lengths. For the  $y$ -oriented junction, the spin-space symmetry  $[U_s|C_{4z}]$  yields analogous results, but with only the spin- $\downarrow$  channel carrying the supercurrent. Thus, for  $\text{CsV}_2\text{Te}_2\text{O}$ -based junctions, we conclude:

$$\begin{cases} x\text{-direction junction, only } I_{\uparrow\uparrow}^x \text{ is finite,} \\ y\text{-direction junction, only } I_{\downarrow\downarrow}^y \text{ is finite.} \end{cases} \quad (6)$$

We term this phenomenon the *spin-selective Josephson effect*. Moreover,  $[U_s|C_{4z}]$  enforces  $I_{\uparrow\uparrow}^x = I_{\downarrow\downarrow}^y$ . These results establish a route toward dissipationless spin control in superconducting spintronic devices.

To quantify the spin-selectivity and distinguish the altermagnetic state from ferromagnetic orders, we define the spin supercurrents for the two junction orientations,

$$I_{\text{spin}}^{x/y} = I_{\uparrow\uparrow}^{x/y} - I_{\downarrow\downarrow}^{x/y}, \quad (7)$$

which directly probes the altermagnetic response to an external magnetic field. For clarity, we consider four representative magnetic configurations (neglecting transition processes): (i) a ferromagnet with majority spin  $\uparrow$ ; (ii) an altermagnet with Néel vector along  $+\hat{z}$ ; (iii) an altermagnet with Néel vector along  $-\hat{z}$ ; and (iv) a ferromagnet with majority spin  $\downarrow$ . These phases can, in principle, be tuned by an out-of-plane magnetic field applied to the  $\text{CsV}_2\text{Te}_2\text{O}$  layer, assuming the superconducting leads remain essentially unaffected [92]. The results are summarized in Fig 2(e). In the altermagnetic state, the spin supercurrents along the two orthogonal directions are opposite in sign,  $I_{\text{spin}}^x = -I_{\text{spin}}^y$ . Reversing the Néel vector flips the sign of both  $I_{\text{spin}}^x$  and  $I_{\text{spin}}^y$ . In contrast, when the field drives the system into a ferromagnetic state, the two spin supercurrents become equal, indicating that the spin-polarized supercurrent propagates isotropically, independent of the junction orientation.

Therefore, we conclude that the spin-selective Josephson effect constitutes a unique signature of the  $\text{CsV}_2\text{Te}_2\text{O}$  family hidden altermagnets, distinct from all previously reported behaviors in altermagnet-based Josephson junctions [22–25, 78, 93–99].

### Phase diagram for bilayer system

We next study the bilayer system. As noted, the symmetry  $[U_s|M_z]$  distinguishes the monolayer from the bilayer system—the latter being another important structural unit for  $\text{CsV}_2\text{Te}_2\text{O}$ . This symmetry “hides” the

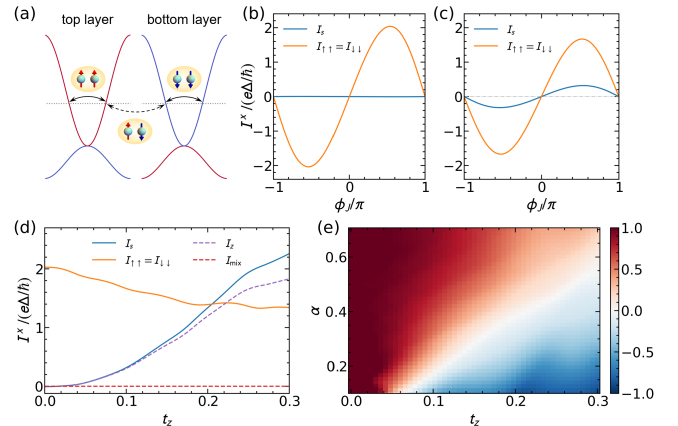


FIG. 3. Planar junctions in bilayer  $\text{CsV}_2\text{Te}_2\text{O}$ . (a) Schematic of layer-resolved spin-split bands in the top and bottom layers. Proximity-induced superconducting pairings include intra-layer equal-spin triplet and inter-layer opposite-spin triplet pairing, the latter mediated by the inter-layer hopping  $t_z$ . (b)-(c) Supercurrent components in a long junction ( $L_{\text{AM}} = 50$ ) for two cases: (b) For  $t_z = 0.01$  eV, the spin-singlet supercurrent  $I_s^x$  is negligible. (c) For  $t_z = 0.1$  eV,  $I_s^x$  becomes comparable to the equal-spin triplet components  $I_{\uparrow\uparrow}^x = I_{\downarrow\downarrow}^x$ . (d) Dependence of all supercurrent components on  $t_z$  at  $\alpha = 0.4$  and  $\phi_J = \pi/2$ . (e) Normalized supercurrent difference  $\Delta I_{\text{JJ}}^x / I_{\text{tot}}^x$  in the  $t_z$ - $\alpha$  plane, where  $\Delta I_{\text{JJ}}^x$  is defined in Eq. (9).

altermagnetic spin-splitting in the bilayer, thereby suppressing the *spin-selective Josephson effect* found in the monolayer [Eq. (6)]. Nevertheless, an equal-spin-triplet supercurrent persists for bilayer junctions along both the  $x$  and  $y$  directions. As illustrated in Fig. 3(a), equal-spin-triplet pairing correlations are induced separately in each layer:  $\hat{F}_{\uparrow\uparrow}$  in the top layer and  $\hat{F}_{\downarrow\downarrow}$  in the bottom layer. Crucially, additional supercurrent-carrying channels arise from inter-layer spin-singlet and opposite-spin-triplet pairing correlations. These channels are controlled by the inter-layer hopping  $t_z$ . For  $t_z = 0$ , the bilayer behaves as two independent altermagnetic layers and the additional channels vanish, as expected. As  $t_z$  increases to values comparable to the intra-layer hoppings, the system crosses over to the bulk limit, where singlet and triplet pairings coexist. To investigate this  $t_z$ -driven crossover, we consider the bilayer Hamiltonian

$$\mathcal{H}_{\text{bAM}}(\mathbf{k}) = [\epsilon_{2+} + \epsilon_3 - \mu] \hat{\gamma}_0 \hat{\sigma}_0 \hat{s}_0 + \epsilon_{2-} \hat{\gamma}_0 \hat{\sigma}_z \hat{s}_0 + \epsilon_1 \hat{\gamma}_0 \hat{\sigma}_x \hat{s}_0 + M \hat{\gamma}_z \hat{\sigma}_z \hat{s}_z + t_z \hat{\gamma}_x \hat{\sigma}_0 \hat{s}_0, \quad (8)$$

where  $\hat{\gamma}_\mu$  are Pauli matrices acting on the layer degree of freedom. The energy spectrum remains spin-degenerate. We calculate the Josephson supercurrent along the  $x$  direction for the bilayer junction. To suppress intra-layer contributions to the spin-singlet supercurrent, we consider a long junction of length  $L_{\text{AM}} = 50$ . In the weak inter-layer coupling regime ( $t_z = 0.01$  eV), the supercurrent is dominated by equal-spin-triplet pairings, with a negligible spin-singlet contribution  $I_s^x$  [Fig. 3(b)]. No-

table, we confirm  $I_{\uparrow\uparrow}^x = I_{\downarrow\downarrow}^x$ , a direct consequence of the G-type antiferromagnetic order. When  $t_z$  increases to 0.1 eV,  $I_s^x$  becomes significant, though still smaller than  $I_{\uparrow\uparrow}^x$  [Fig. 3(c)]. This indicates that enhanced inter-layer hybridization can dramatically tune the supercurrent composition in bilayer junctions.

To elucidate the microscopic origin of this evolution, Fig. 3(d) shows all supercurrent components  $I_m^x(\pi/2)$  with  $m = \{s, \uparrow\uparrow, \downarrow\downarrow, z, \text{mix}\}$  as a function of  $t_z$ . As  $t_z$  increases, the intra-layer equal-spin-triplet supercurrents ( $I_{\uparrow\uparrow}^x = I_{\downarrow\downarrow}^x$ ) remain robust, while both the spin-singlet supercurrent  $I_s^x$  and the opposite-spin-triplet supercurrent  $I_z^x$  are progressively enhanced. Moreover, since  $t_z \leq 0.3$  eV remains smaller than the altermagnetic spin-splitting strength ( $|M| = 0.9$  eV), the equal-spin-triplet supercurrents exhibit only weak variation. However,  $I_{\text{mix}}^x$  remains exactly zero owing to the absence of spin-dependent hopping parameters in the altermagnet (see Methods).

Beyond the tuning of singlet-triplet components via  $t_z$ , the Rashba spin-orbit coupling  $\alpha$  in the  $s$ -wave superconducting leads also governs the conversion between singlet and triplet pairings. To map out the supercurrent composition, we construct a two-dimensional phase diagram in the  $t_z$ - $\alpha$  plane [Fig. 3(e)]. We quantify the competition by defining

$$\Delta I_{\text{JJ}}^x = I_{\text{eq}}^x - I_{\text{op}}^x, \quad (9)$$

where  $I_{\text{eq}}^x = I_{\uparrow\uparrow}^x + I_{\downarrow\downarrow}^x$  and  $I_{\text{op}}^x = I_s^x + I_z^x + I_{\text{mix}}^x$  denote the supercurrent contributions from pairings with total spin angular momentum  $\pm 1$  and 0, respectively. Figure 3(e) shows the normalized supercurrent difference  $\Delta I_{\text{JJ}}^x/I_{\text{tot}}^x$ . The Josephson supercurrent is dominated by equal-spin-triplet pairings in the regime of large  $\alpha$  but small  $t_z$  ( $I_{\text{eq}}^x \gg I_{\text{op}}^x$ ). In contrast, for small  $\alpha$  but large  $t_z$ , the spin-singlet supercurrent becomes dominant ( $I_{\text{op}}^x \approx I_s^x \gg I_{\text{eq}}^x$ ). In practice, uniaxial strain along the [001] direction could provide a way to control  $t_z$ , enabling a controlled crossover between triplet-dominated and singlet-dominated supercurrents.

The inter-layer hopping in unstrained  $\text{CsV}_2\text{Te}_2\text{O}$  is only 0.01 eV [73], firmly placing the system within the weak-coupling regime. Therefore, we conclude that equal-spin-triplet supercurrents dominate in bilayer  $\text{CsV}_2\text{Te}_2\text{O}$ -based Josephson junctions, despite the material being in a G-type antiferromagnetic phase.

### Altermagnetic even-odd effect

The preceding sections reveal a striking and, to our knowledge, previously unrecognized phenomenon: the Josephson effect in hidden altermagnets is governed fundamentally by layer parity. In the monolayer, the altermagnetic spin splitting yields a fully spin-selective supercurrent—only  $I_{\uparrow\uparrow}^x$  (or  $I_{\downarrow\downarrow}^y$ ) carries the charge. In the bilayer, this selectivity is hidden by the symmetry [ $U_s|M_z$ ], yet equal-spin-triplet supercurrents ( $I_{\uparrow\uparrow}^x = I_{\downarrow\downarrow}^x$  and  $I_{\uparrow\uparrow}^y = I_{\downarrow\downarrow}^y$ ) persist and dominate as long as the inter-

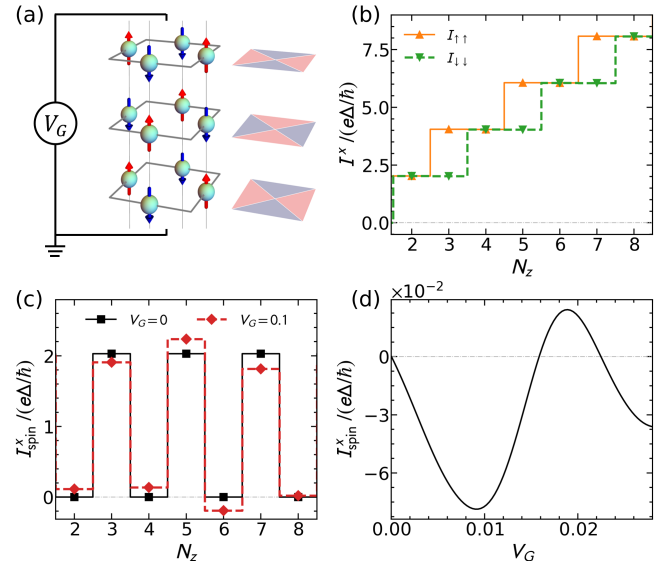


FIG. 4. Altermagnetic even-odd effect in  $\text{CsV}_2\text{Te}_2\text{O}$  with small inter-layer hopping  $t_z = 0.01$  eV. (a) Schematic illustration of the planar junction for the multilayer structure. A gate voltage is applied perpendicular to the altermagnetic planes. (b) Layer-parity dependence of  $I_{\uparrow\uparrow}^x$  and  $I_{\downarrow\downarrow}^x$  at  $\phi_J = \pi/2$ . (c) The corresponding spin current  $I_{\text{spin}}^x = I_{\uparrow\uparrow}^x - I_{\downarrow\downarrow}^x$ , showing on-off switching by adding layers ( $V_G = 0$ , black curve). A finite gate voltage ( $V_G = 0.1$  eV) induces a spin supercurrent in even- $N_z$  systems (red curve). (d) Nonmonotonic dependence of the spin current  $I_{\text{spin}}^x$  on gate voltage  $V_G$  for a four-layer junction ( $N_z = 4$ ).

layer hopping remains weak. We unify these distinct phenomena under the concept of an *altermagnetic even-odd effect*: the layer-number parity fundamentally dictates the symmetry and spin polarization of the supercurrent in multilayer systems. Thus, we consider an  $N_z$ -layered  $\text{CsV}_2\text{Te}_2\text{O}$  films described by,

$$\mathcal{H}_{\text{mAM}}(\mathbf{k}) = [\epsilon_{2+} + \epsilon_3 - \mu] \hat{\Gamma}_0 \hat{\sigma}_0 \hat{s}_0 + \epsilon_{2-} \hat{\Gamma}_0 \hat{\sigma}_z \hat{s}_0 + \epsilon_1 \hat{\Gamma}_0 \hat{\sigma}_x \hat{s}_0 + M \hat{\Gamma}_z \hat{\sigma}_z \hat{s}_z + t_z \hat{\Gamma}_x \hat{\sigma}_0 \hat{s}_0, \quad (10)$$

where  $\hat{\Gamma}_0$  is the  $N_z \times N_z$  identity matrix,  $\hat{\Gamma}_z = \text{diag}[1, -1, 1, -1, \dots, (-1)^{N_z+1}]$  encodes the alternating layer magnetization, and  $\hat{\Gamma}_x$  is an  $N_z \times N_z$  symmetric tridiagonal matrix representing inter-layer hopping (ones on the first sub- and super-diagonals, zeros elsewhere). Notice that the system carries zero net magnetization. Using a multilayer Josephson junction platform with an electrostatic gate  $V_G$  [Fig. 4(a)], we demonstrate how the superconducting transport evolves with layer parity, thereby establishing the *altermagnetic even-odd effect* as a general and tunable design principle for altermagnet-based superconducting devices.

We now focus on  $x$ -oriented junctions. In Fig. 4(b), we present the equal-spin-triplet supercurrent components,  $I_{\uparrow\uparrow}^x(N_z)$  and  $I_{\downarrow\downarrow}^x(N_z)$  at  $\phi_J = \pi/2$ , as functions of  $N_z$ . For even  $N_z$ , the two components are exactly equal,

$I_{\uparrow\uparrow}^x(N_z) = I_{\downarrow\downarrow}^x(N_z)$ , yielding a vanishing net spin supercurrent,  $I_{\text{spin}}^x(N_z) = 0$ . The spin-singlet contributions remain negligible as we consider the small inter-layer coupling  $t_z$ . For odd  $N_z$ , the spin balance is broken, and the supercurrent obeys the following parity relations,

$$I_{\uparrow\uparrow}^x(N_z) = I_{\uparrow\uparrow}^x(N_z + 1), \quad (11a)$$

$$I_{\downarrow\downarrow}^x(N_z) = I_{\downarrow\downarrow}^x(N_z - 1). \quad (11b)$$

Likewise, junctions oriented along the  $y$  direction exhibit fully analogous behavior, with the roles of spin-up and spin-down currents exchanged. Thus, the relative magnitude of  $I_{\uparrow\uparrow}^{x/y}$  and  $I_{\downarrow\downarrow}^{x/y}$  is a sensitive probe of layer parity—directly reflecting the alternating spin texture of the hidden altermagnetic order in  $\text{CsV}_2\text{Te}_2\text{O}$  films.

To further quantify the even-odd switching, we plot the net spin supercurrent  $I_{\text{spin}}^x$  in Fig. 4(c). The layer number  $N_z$  acts as a spin-current switch (solid curve):  $I_{\text{spin}}^x$  is finite for odd  $N_z$  (“on”) and vanishes for even  $N_z$  (“off”). This parity-controlled signal can be further manipulated by an external gate voltage  $V_G$  [100], as illustrated in Fig. 4(a), which breaks the spin-space symmetry [ $U_s|M_z$ ] and thereby activates a finite  $I_{\text{spin}}^x$  even in even- $N_z$  systems (see Methods for modeling details). The dashed curve in Fig. 4(c) shows the result for  $V_G = 0.1$  eV. Strikingly, the gate-induced spin supercurrent in even- $N_z$  systems exhibits a nonmonotonic dependence on thickness. This behavior originates from a more fundamental nonmonotonic response of  $I_{\text{spin}}^x$  to  $V_G$  [see Fig. 4(d) for the  $N_z = 4$  case], which arises from finite-momentum Cooper pairing.

The altermagnetic even-odd effect in the  $\text{CsV}_2\text{Te}_2\text{O}$  family is distinct from the even-odd effects reported in topological antiferromagnetic  $\text{MnBi}_2\text{Te}_4$  films [101–106]. The latter originates from surface-state topology and exhibits a net magnetization in odd layers that vanishes in even layers; the former, in contrast, arises purely from hidden altermagnetism and yields zero net magnetization in both odd and even layers. Namely, the even-odd effect in  $\text{MnBi}_2\text{Te}_4$  is reflected in its net magnetization, while in  $\text{CsV}_2\text{Te}_2\text{O}$  it is reflected in its net altermagnetism. Our results thus establish an entirely different physical mechanism and a new material platform for parity-controlled superconducting spintronics.

## Discussion and conclusion

*Material realization and experimental signatures.*—This  $\text{CsV}_2\text{Te}_2\text{O}$  family is believed to be hidden altermagnet, and our results on  $\text{CsV}_2\text{Te}_2\text{O}$  can be applied to other materials in this family. Our effective model for monolayer  $\text{CsV}_2\text{Te}_2\text{O}$  includes only the  $d_{xz}$  and  $d_{yz}$  orbitals and omits the Fermi surfaces near  $X$  and  $Y$  points. We discuss three points that support the robustness of our conclusions despite this simplification: (i) The impurity-induced bound states recently observed by scanning tunneling microscopy [74–76] originate from quasi-1D near-flat segments of the Fermi surface. (ii)

These additional Fermi surfaces can, in principle, be eliminated via electrostatic gating or chemical substitution in altermagnetic thin films. (iii) Even if present, these Fermi surfaces also carry spin-polarized supercurrents that are fully consistent with—and do not alter—our central conclusions regarding the spin-selective and even-odd Josephson effects. More broadly, the altermagnetic even-odd effect is not limited to Josephson junctions; it can be extended to a wide range of magnetic and transport phenomena, including spin injection, magnetoresistance, and nonlocal correlations. The even-odd effect in Josephson junctions may be directly accessible via differential conductance spectra [107] and microwave spectroscopy [108], or indirectly probed through spin-polarized Andreev bound states detected by scanning tunneling microscopy [109]—a direction we leave for future work.

*Even-odd effect in vertical junctions.*—While the preceding analysis focuses on planar junctions, the altermagnetic even-odd effect is not limited to this geometry. Vertical Josephson junctions—where the supercurrent flows perpendicular to the altermagnetic layers—offer an alternative and technologically relevant platform. When the inter-layer hopping  $t_z$  is sufficiently large, transport along the vertical direction becomes appreciable. To be concrete, we consider a Josephson junction oriented along  $z$ , in which an  $N_z$ -layer altermagnet with G-type antiferromagnetic order [Eq. (10)] is sandwiched between two Rashba superconductors [Fig. 5(a), inset]. We assume in-plane translational symmetry so that  $k_x$  and  $k_y$  remain good quantum numbers. In this geometry, the symmetry [ $U_s||C_{4z}$ ] is preserved. Consequently, the two spin channels are symmetry-related and no spin-selective Josephson effect appears. Nevertheless, the interplay between  $t_z$  in the altermagnet and  $\alpha$  in the Rashba superconduct-

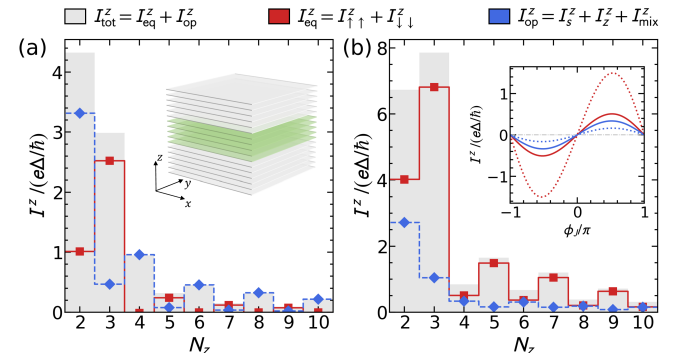


FIG. 5. Altermagnetic even-odd effect in vertical Josephson junctions. (a) Layer dependence of the equal-spin triplet supercurrent  $I_{\text{eq}}^z$  and opposite-spin supercurrent  $I_{\text{op}}^z$  at  $\phi_J = \pi/2$  and  $\alpha = 0.1$ . Gray-shaded rectangles represent the total supercurrent. Inset: schematic of the vertical junction. (b) Same as (a) but for  $\alpha = 0.4$ . Inset: current-phase relation for  $N_z = 4$  (solid curve) and  $N_z = 5$  (dotted curve). Here,  $t_z = 0.2$  is used to emphasize the even-odd effect.

ing leads enables both equal-spin triplet and opposite-spin pairing correlations to be induced and transmitted across the junction. This suggests the possibility of a pronounced even-odd layer dependence. To explore this, we calculate the equal-spin triplet ( $I_{\text{eq}}^z = I_{\uparrow\uparrow}^z + I_{\downarrow\downarrow}^z$ ) and opposite-spin ( $I_{\text{op}}^z = I_s^z + I_z^z + I_{\text{mix}}^z$ ) contributions to the supercurrent at  $\phi_J = \pi/2$  as functions of  $N_z$  [Fig. 5].

Our calculations reveal a clear even-odd dichotomy: odd- $N_z$  junctions enhance  $I_{\text{eq}}^z$  while suppressing  $I_{\text{op}}^z$ . This behavior stems from the net altermagnetic spin splitting present in odd-layer barriers, which facilitates the propagation of equal-spin triplet pairs but disrupts opposite-spin transport. By contrast, even- $N_z$  junctions host spin-degenerate bands, and thus favor opposite-spin pairing. These even-odd contrasts are robust in the weak spin-orbit coupling regime:  $\alpha < t_z$ .

Explicitly,  $I_{\text{eq}}^z$  is enhanced for odd  $N_z$  but strongly suppressed for even  $N_z$  [blue solid line in Fig. 5(a)]. Conversely,  $I_{\text{op}}^z$  is enhanced for even  $N_z$  and suppressed for odd  $N_z$  [red dashed line in Fig. 5(a)]. As a result, on top of the overall decay, the total current  $I_{\text{tot}}^z = I_{\text{eq}}^z + I_{\text{op}}^z$  oscillates with period two as increasing  $N_z$ : larger for even layers and smaller for odd layers.

This even-odd effect persists in the strong spin-orbit coupling regime ( $\alpha > t_z$ ), with the key distinction that equal-spin triplet pairs now carry the majority of the supercurrent [Fig. 5(b)]. Consequently, the total current becomes stronger for odd layers and weaker for even layers. Although we present results at  $\phi_J = \pi/2$ , the even-odd effect holds across other phase differences, as evidenced by the current-phase relations in the inset of Fig. 5(b). For clarity, we present the results at an enhanced  $t_z$ ; the same qualitative features persist for smaller  $t_z$ , albeit with faster decay as  $N_z$  increases.

*Conclusion.*— We have uncovered a family of altermagnetic even-odd effects in Josephson junctions based on  $\text{CsV}_2\text{Te}_2\text{O}$ —a van der Waals  $d$ -wave altermagnet with G-type antiferromagnetic order. In planar junctions, the quasi-1D, spin-polarized Fermi surfaces with flat segments yields a fully spin-polarized, directionally anisotropic supercurrent that survives only in odd-layer systems; even-layer junctions exhibit exact cancellation of the spin supercurrent. Thus, layer parity acts as a switch for spin-polarized supercurrent. In vertical junctions, odd layers favor equal-spin triplet transport while even layers favor opposite-spin transport, giving rise to a robust period-two oscillation in the total supercurrent. These layer-parity-controlled responses constitute a generic even-odd phenomenon intrinsic to hidden altermagnets, distinct from conventional even-odd effects in antiferromagnetic or nonmagnetic multilayers. Our theory can also be applied to other magnetic materials, such as X-type antiferromagnets [44].

We thank G.-W. Yang, X. Lu, L. Jiao, H.-M. Yi, Z.-Y. Zhang and F.-C. Zhang for helpful discussions. C.L. and L.H.H. were supported by National Key R&D Pro-

gram of China (Grant No. 2025YFA1411501), the National Natural Science Foundation of China (Grant Nos. 12561160109, 1257040632), the Fundamental Research Funds for the Central Universities (Grant No. 226-2024-00068). C.L. was also supported by central fiscal special-purpose fund (Grant No. 2021ZD0302500). J.X.H. and S.B.Z. were supported by the start-up fund at HFNL, the National Natural Science Foundation of China (Grant No. 12488101) and the Innovation Program for Quantum Science and Technology (Grant No. 2021ZD0302801).

\* These authors contributed equally.

† songbozhang@ustc.edu.cn

‡ lunhui@zju.edu.cn

- [1] J. E. Hirsch, Spin-split states in metals, *Phys. Rev. B* **41**, 6820 (1990).
- [2] H. Ikeda and Y. Ohashi, Theory of unconventional spin density wave: A possible mechanism of the micromagnetism in u-based heavy fermion compounds, *Phys. Rev. Lett.* **81**, 3723 (1998).
- [3] C. Wu and S.-C. Zhang, Dynamic generation of spin-orbit coupling, *Phys. Rev. Lett.* **93**, 036403 (2004).
- [4] C. Wu, K. Sun, E. Fradkin, and S.-C. Zhang, Fermi liquid instabilities in the spin channel, *Phys. Rev. B* **75**, 115103 (2007).
- [5] H. Chen, Q. Niu, and A. H. MacDonald, Anomalous hall effect arising from noncollinear antiferromagnetism, *Phys. Rev. Lett.* **112**, 017205 (2014).
- [6] S. Nakatsuji, N. Kiyohara, and T. Higo, Large anomalous hall effect in a non-collinear antiferromagnet at room temperature, *Nature* **527**, 212 (2015).
- [7] Y. Noda, K. Ohno, and S. Nakamura, Momentum-dependent band spin splitting in semiconducting  $\text{MnO}_2$ : a density functional calculation, *Physical Chemistry Chemical Physics* **18**, 13294 (2016).
- [8] K.-H. Ahn, A. Hariki, K.-W. Lee, and J. Kuneš, Antiferromagnetism in  $\text{ruo}_2$  as  $d$ -wave pomeranchuk instability, *Phys. Rev. B* **99**, 184432 (2019).
- [9] Q. Liu, X. Dai, and S. Blügel, Different facets of unconventional magnetism, *Nature Physics* **21**, 329 (2025).
- [10] Z. Liu, M. Wei, W. Peng, D. Hou, Y. Gao, and Q. Niu, Multipolar anisotropy in anomalous hall effect from spin-group symmetry breaking, *Phys. Rev. X* **15**, 031006 (2025).
- [11] Y. Liu, X. Chen, Y. Yu, and Q. Liu, Symmetry classification of magnetic orders and emergence of spin-orbit magnetism, *arXiv preprint arXiv:2506.20739* (2025).
- [12] L. Šmejkal, R. González-Hernández, T. Jungwirth, and J. Sinova, Crystal time-reversal symmetry breaking and spontaneous Hall effect in collinear antiferromagnets, *Sci. Adv.* **6**, eaaz8809 (2020).
- [13] M. Naka, S. Hayami, H. Kusunose, Y. Yanagi, Y. Motome, and H. Seo, Spin current generation in organic antiferromagnets, *Nat. Commun.* **10**, 4305 (2019).
- [14] M. Naka, Y. Motome, and H. Seo, Perovskite as a spin current generator, *Phys. Rev. B* **103**, 125114 (2021).
- [15] S. Hayami, Y. Yanagi, and H. Kusunose, Momentum-dependent spin splitting by collinear antiferromagnetic ordering, *J. Phys. Soc. Jpn.* **88**, 123702 (2019).

[16] L.-D. Yuan, Z. Wang, J.-W. Luo, E. I. Rashba, and A. Zunger, Giant momentum-dependent spin splitting in centrosymmetric low- $Z$  antiferromagnets, *Phys. Rev. B* **102**, 014422 (2020).

[17] I. I. Mazin, K. Koepernik, M. D. Johannes, R. González-Hernández, and L. Šmejkal, Prediction of unconventional magnetism in doped FeSb<sub>2</sub>, *Proc. Nat. Acad. Sci. USA* **118**, e2108924118 (2021).

[18] H.-Y. Ma, M. Hu, N. Li, J. Liu, W. Yao, J.-F. Jia, and J. Liu, Multifunctional antiferromagnetic materials with giant piezomagnetism and noncollinear spin current, *Nat. Commun.* **12**, 2846 (2021).

[19] D.-F. Shao, S.-H. Zhang, M. Li, C.-B. Eom, and E. Y. Tsymbal, Spin-neutral currents for spintronics, *Nat. Commun.* **12**, 7061 (2021).

[20] L. Šmejkal, J. Sinova, and T. Jungwirth, Beyond conventional ferromagnetism and antiferromagnetism: A phase with nonrelativistic spin and crystal rotation symmetry, *Phys. Rev. X* **12**, 031042 (2022).

[21] L. Šmejkal, J. Sinova, and T. Jungwirth, Emerging research landscape of altermagnetism, *Phys. Rev. X* **12**, 040501 (2022).

[22] J. A. Ouassou, A. Brataas, and J. Linder, dc josephson effect in altermagnets, *Phys. Rev. Lett.* **131**, 076003 (2023).

[23] S.-B. Zhang, L.-H. Hu, and T. Neupert, Finite-momentum Cooper pairing in proximitized altermagnets, *Nat. Commun.* **15**, 1801 (2024).

[24] C. W. J. Beenakker and T. Vakhtel, Phase-shifted andreev levels in an altermagnet josephson junction, *Phys. Rev. B* **108**, 075425 (2023).

[25] Q. Cheng and Q.-F. Sun, Orientation-dependent josephson effect in spin-singlet superconductor-altermagnet-spin-triplet superconductor junctions, *Phys. Rev. B* **109**, 024517 (2024).

[26] T. A. Maier and S. Okamoto, Weak-coupling theory of neutron scattering as a probe of altermagnetism, *Phys. Rev. B* **108**, L100402 (2023).

[27] R. He, D. Wang, N. Luo, J. Zeng, K.-Q. Chen, and L.-M. Tang, Nonrelativistic spin-momentum coupling in antiferromagnetic twisted bilayers, *Phys. Rev. Lett.* **130**, 046401 (2023).

[28] D. Zhu, Z.-Y. Zhuang, Z. Wu, and Z. Yan, Topological superconductivity in two-dimensional altermagnetic metals, *Phys. Rev. B* **108**, 184505 (2023).

[29] V. Leeb, A. Mook, L. Šmejkal, and J. Knolle, Spontaneous formation of altermagnetism from orbital ordering, *Phys. Rev. Lett.* **132**, 236701 (2024).

[30] L.-D. Yuan, A. B. Georgescu, and J. M. Rondinelli, Nonrelativistic spin splitting at the brillouin zone center in compensated magnets, *Phys. Rev. Lett.* **133**, 216701 (2024).

[31] M. Roig, A. Kreisel, Y. Yu, B. M. Andersen, and D. F. Agterberg, Minimal models for altermagnetism, *Phys. Rev. B* **110**, 144412 (2024).

[32] Y. Liu, J. Yu, and C.-C. Liu, Twisted magnetic van der waals bilayers: An ideal platform for altermagnetism, *Phys. Rev. Lett.* **133**, 206702 (2024).

[33] M. Gu, Y. Liu, H. Zhu, K. Yananose, X. Chen, Y. Hu, A. Stroppa, and Q. Liu, Ferroelectric switchable altermagnetism, *Phys. Rev. Lett.* **134**, 106802 (2025).

[34] C. Xu, S. Wu, G.-X. Zhi, G. Cao, J. Dai, C. Cao, X. Wang, and H.-Q. Lin, Altermagnetic ground state in distorted kagome metal CsCr<sub>3</sub>Sb<sub>5</sub>, *Nat. Commun.* **16**, 3114 (2025).

[35] D. Chakraborty and A. M. Black-Schaffer, Perfect superconducting diode effect in altermagnets, *Phys. Rev. Lett.* **135**, 026001 (2025).

[36] X. Duan, J. Zhang, Z. Zhu, Y. Liu, Z. Zhang, I. Žutić, and T. Zhou, Antiferroelectric altermagnets: Antiferroelectricity alters magnets, *Phys. Rev. Lett.* **134**, 106801 (2025).

[37] H.-J. Lin, S.-B. Zhang, H.-Z. Lu, and X. C. Xie, Coulomb drag in altermagnets, *Phys. Rev. Lett.* **134**, 136301 (2025).

[38] Z.-M. Wang, Y. Zhang, S.-B. Zhang, J.-H. Sun, E. Dagotto, D.-H. Xu, and L.-H. Hu, Spin-orbital altermagnetism, *Phys. Rev. Lett.* **135**, 176705 (2025).

[39] M. Vila, V. Sunko, and J. E. Moore, Orbital-spin locking and its optical signatures in altermagnets, *Phys. Rev. B* **112**, L020401 (2025).

[40] G. Sim and J. Knolle, Pair density waves and supercurrent diode effect in altermagnets, *Phys. Rev. B* **112**, L020502 (2025).

[41] Y.-M. Wu, Y. Wang, and R. M. Fernandes, Intra-unit-cell singlet pairing mediated by altermagnetic fluctuations, *Phys. Rev. Lett.* **135**, 156001 (2025).

[42] X. Zhu, X. Huo, S. Feng, S.-B. Zhang, S. A. Yang, and H. Guo, Design of Altermagnetic Models from Spin Clusters, *Phys. Rev. Lett.* **134**, 166701 (2025).

[43] R. Chen, Z.-M. Wang, K. Wu, H.-P. Sun, B. Zhou, R. Wang, and D.-H. Xu, Probing  $\mathbf{k}$ -space alternating spin polarization via the anomalous hall effect, *Phys. Rev. Lett.* **135**, 096602 (2025).

[44] S.-S. Zhang, Z.-A. Wang, B. Li, Y.-Y. Jiang, S.-H. Zhang, R.-C. Xiao, L.-X. Liu, X. Luo, W.-J. Lu, M. Tian, Y.-P. Sun, E. Y. Tsymbal, H. Du, and D.-F. Shao, X-type stacking in cross-chain antiferromagnets, *Newton* **1**, 100068 (2025).

[45] Z. Feng, X. Zhou, L. Šmejkal, L. Wu, Z. Zhu, H. Guo, R. González-Hernández, X. Wang, H. Yan, P. Qin, X. Zhang, H. Wu, H. Chen, Z. Meng, L. Liu, Z. Xia, J. Sinova, T. Jungwirth, and Z. Liu, An anomalous hall effect in altermagnetic ruthenium dioxide, *Nature Electronics* **5**, 735–743 (2022).

[46] R. Gonzalez Betancourt, J. Zubáč, R. Gonzalez-Hernandez, K. Geishendorf, Z. Šobáň, G. Springholz, K. Olejník, L. Šmejkal, J. Sinova, T. Jungwirth, et al., Spontaneous anomalous hall effect arising from an unconventional compensated magnetic phase in a semiconductor, *Phys. Rev. Lett.* **130**, 036702 (2023).

[47] S. Lee, S. Lee, S. Jung, J. Jung, D. Kim, Y. Lee, B. Seok, J. Kim, B. G. Park, L. Šmejkal, et al., Broken kramers degeneracy in altermagnetic MnTe, *Phys. Rev. Lett.* **132**, 036702 (2024).

[48] J. Krempaský, L. Šmejkal, S. D’souza, M. Hajlaoui, G. Springholz, K. Uhlířová, F. Alarab, P. Constantinou, V. Strocov, D. Usanov, et al., Altermagnetic lifting of kramers spin degeneracy, *Nature* **626**, 517 (2024).

[49] T. Osumi, S. Souma, T. Aoyama, K. Yamauchi, A. Honma, K. Nakayama, T. Takahashi, K. Ohgushi, and T. Sato, Observation of a giant band splitting in altermagnetic MnTe, *Phys. Rev. B* **109**, 115102 (2024).

[50] W. Lu, S. Feng, Y. Wang, D. Chen, Z. Lin, X. Liang, S. Liu, W. Feng, K. Yamagami, J. Liu, et al., Signature of topological surface bands in altermagnetic weyl semimetal CrSb, *Nano Letters* **25**, 7343 (2025).

[51] O. Fedchenko, J. Minár, A. Akashdeep, S. W. D’Souza,

D. Vasilyev, O. Tkach, L. Odenbreit, Q. Nguyen, D. Kutnyakhov, N. Wind, et al., Observation of time-reversal symmetry breaking in the band structure of altermagnetic RuO<sub>2</sub>, *Science advances* **10**, eadj4883 (2024).

[52] Z. Lin, D. Chen, W. Lu, X. Liang, S. Feng, K. Yamagami, J. Osiecki, M. Leandersson, B. Thiagarajan, J. Liu, et al., Observation of giant spin splitting and d-wave spin texture in room temperature altermagnet RuO<sub>2</sub>, *arXiv:2402.04995* (2024).

[53] Z. Liu, M. Ozeki, S. Asai, S. Itoh, and T. Masuda, Chiral split magnon in altermagnetic MnTe, *Phys. Rev. Lett.* **133**, 156702 (2024).

[54] S. Reimers, L. Odenbreit, L. Šmejkal, V. N. Strocov, P. Constantinou, A. B. Hellenes, R. Jaeschke Ubiergo, W. H. Campos, V. K. Bharadwaj, A. Chakraborty, et al., Direct observation of altermagnetic band splitting in CrSb thin films, *Nat. Commun.* **15**, 2116 (2024).

[55] J. Ding, Z. Jiang, X. Chen, Z. Tao, Z. Liu, T. Li, J. Liu, J. Sun, J. Cheng, J. Liu, et al., Large band splitting in g-wave altermagnet crsb, *Phys. Rev. Lett.* **133**, 206401 (2024).

[56] L. Han, X. Fu, R. Peng, X. Cheng, J. Dai, L. Liu, Y. Li, Y. Zhang, W. Zhu, H. Bai, et al., Electrical 180 switching of Néel vector in spin-splitting antiferromagnet, *Science Advances* **10**, eadn0479 (2024).

[57] Z. Zhou, X. Cheng, M. Hu, R. Chu, H. Bai, L. Han, J. Liu, F. Pan, and C. Song, Manipulation of the altermagnetic order in crsb via crystal symmetry, *Nature* **638**, 645 (2025).

[58] G. Yang, Z. Li, S. Yang, J. Li, H. Zheng, W. Zhu, Z. Pan, Y. Xu, S. Cao, W. Zhao, et al., Three-dimensional mapping of the altermagnetic spin splitting in CrSb, *Nat. Commun.* **16**, 1442 (2025).

[59] R. B. Regmi, H. Bhandari, B. Thapa, Y. Hao, N. Sharma, J. McKenzie, X. Chen, A. Nayak, M. El Gazzah, B. G. Márkus, et al., Altermagnetism in the layered intercalated transition metal dichalcogenide CoNb<sub>4</sub>Se<sub>8</sub>, *Nat. Commun.* **16**, 4399 (2025).

[60] L.-J. Zhou, Z.-J. Yan, H. Rong, Y. Zhao, P. Xiao, L.-K. Lai, Z. Xi, K. Wang, T. Adhikari, G. P. Tiwari, Z. Lin, P. Manue, F. Orlandi, D. Khalyavin, A. J. Grutter, C.-X. Liu, B. Yan, and C.-Z. Chang, Surface-state-driven anomalous hall effect in altermagnetic MnTe films, *arXiv preprint arXiv:2602.09363* (2026).

[61] T.-H. Shao, X. Dai, W. Hu, M.-Y. Zhu, Y. He, L.-H. Yang, J. Liu, M. Yang, X.-R. Liu, J.-J. Shi, T.-Y. Xiao, Y.-J. Hao, X.-M. Ma, Y. Dai, M. Zeng, Q. Gao, G. Wang, J. Li, C. Wang, and C. Liu, Epitaxial growth and anomalous hall effect in high-quality altermagnetic  $\alpha$ -MnTe thin films, *arXiv preprint arXiv:2602.11645* (2026).

[62] L. Bai, W. Feng, S. Liu, L. Šmejkal, Y. Mokrousov, and Y. Yao, Altermagnetism: Exploring new frontiers in magnetism and spintronics, *Advanced Functional Materials* **34**, 2409327 (2024).

[63] S. S. Fender, O. Gonzalez, and D. K. Bediako, Altermagnetism: A chemical perspective, *Journal of the American Chemical Society* **147**, 2257 (2025).

[64] T. Jungwirth, R. M. Fernandes, E. Fradkin, A. H. MacDonald, J. Sinova, and L. Šmejkal, Altermagnetism: an unconventional spin-ordered phase of matter, *Newton* (2025).

[65] C. Song, H. Bai, Z. Zhou, L. Han, H. Reichlova, J. H. Dil, J. Liu, X. Chen, and F. Pan, Altermagnets as a new class of functional materials, *Nature Reviews Materials* **1** (2025).

[66] T. Jungwirth, J. Sinova, R. M. Fernandes, Q. Liu, H. Watanabe, S. Murakami, S. Nakatsuji, and L. Šmejkal, Symmetry, microscopy and spectroscopy signatures of altermagnetism, *Nature* **649**, 837 (2026).

[67] F. Zhang, X. Cheng, Z. Yin, C. Liu, L. Deng, Y. Qiao, Z. Shi, S. Zhang, J. Lin, Z. Liu, et al., Crystal-symmetry-paired spin-valley locking in a layered room-temperature metallic altermagnet candidate, *Nature Physics* **21**, 760 (2025).

[68] B. Jiang, M. Hu, J. Bai, Z. Song, C. Mu, G. Qu, W. Li, W. Zhu, H. Pi, Z. Wei, et al., A metallic room-temperature d-wave altermagnet, *Nature Physics* **21**, 754 (2025).

[69] M. Hu, Z. Song, J. Cheng, G. Qu, Z. Li, Y. Huang, J. Zhu, G. Zhang, D. Tian, L. Chen, et al., Pronounced orbital-selective electron-electron correlation and electron-phonon coupling in V<sub>2</sub>Se<sub>2</sub>O, *arXiv preprint arXiv:2510.04657* (2025).

[70] L. Chen, J. Yue, J. Cheng, J. Bai, Z. Zhang, X. Ma, F. Hong, G. Chen, J.-T. Wang, Z. Wang, et al., Compression-induced magnetic obstructed atomic insulator and spin singlet state in antiferromagnetic KV<sub>2</sub>Se<sub>2</sub>O, *arXiv preprint arXiv:2511.06712* (2025).

[71] C.-C. Liu, J. Li, J.-Y. Liu, J.-Y. Lu, H.-X. Li, Y. Liu, and G.-H. Cao, Physical properties and first-principles calculations of an altermagnet candidate Cs<sub>1- $\delta$</sub> V<sub>2</sub>Te<sub>2</sub>O, *Phys. Rev. B* **112**, 224439 (2025).

[72] Y. Sun, Y. Huang, J. Cheng, S. Zhang, Z. Li, H. Luo, X. Ma, W. Yang, J. Yang, D. Chen, K. Sun, M. Gutmann, S. C. Capelli, F. Shen, J. Hao, L. He, G. Chen, and S. Li, Antiferromagnetic structure of KV<sub>2</sub>Se<sub>2</sub>O: A neutron diffraction study, *Phys. Rev. B* **112**, 184416 (2025).

[73] G. Yang, R. Chen, C. Liu, J. Li, Z. Pan, L. Deng, N. Zheng, Y. Tang, H. Zheng, W. Zhu, et al., Observation of hidden altermagnetism in Cs<sub>1- $\delta$</sub> V<sub>2</sub>Te<sub>2</sub>O, *arXiv preprint arXiv:2512.00972* (2025).

[74] Z. Wang, S. Yu, X. Cheng, X. Xiao, W. Ma, F. Quan, H. Song, K. Zhang, Y. Zhang, Y. Ma, W. Liu, P. Yadav, X. Shi, Z. Wang, Q. Niu, Y. Gao, B. Xiang, J. Liu, Z. Wang, and X. Chen, Atomic-scale spin sensing of a 2D d-wave altermagnet via helical tunneling, *arXiv preprint arXiv:2512.23290* (2025).

[75] D. Fu, L. Yang, K. Xiao, Y. Wang, Z. Wang, Y. Yao, Q.-K. Xue, and W. Li, Atomic-scale visualization of d-wave altermagnetism, *arXiv preprint arXiv:2512.24114* (2025).

[76] L. Jiao, To be submitted..

[77] Q. Hu, X. Cheng, Q. Duan, Y. Hu, B. Jiang, Y. Xiao, Y. Li, M. Pan, L. Deng, C. Liu, et al., Observation of spin-valley locked nodal lines in a quasi-2D altermagnet, *arXiv preprint arXiv:2601.02883* (2026).

[78] C. Li, J.-X. Hou, F.-C. Zhang, S.-B. Zhang, and L.-H. Hu, Spin-polarized josephson supercurrent in nodeless altermagnets, *arXiv preprint arXiv:2509.13838* (2025).

[79] J. Lai, T. Yu, P. Liu, L. Liu, G. Xing, X.-Q. Chen, and Y. Sun, d-wave flat fermi surface in altermagnets enables maximum charge-to-spin conversion, *Phys. Rev. Lett.* **135**, 256702 (2025).

[80] W. Zhang, E. Zhu, Z. Li, and H. Lv, Strain-tunable spin-valley locking and the influence of spin-orbit coupling in

the two-dimensional altermagnet  $V_2Te_2O$ , *Phys. Rev. B* **112**, 144427 (2025).

[81] X. Yan, Z. Song, J. Song, Z. Fang, H. Weng, and Q. Wu, SDW driven “magnetic breakdown” in a d-wave altermagnet  $KV_2Se_2O$ , *arXiv preprint arXiv:2505.00074* (2025).

[82] Y. Nagae, A. P. Schnyder, and S. Ikeyama, Spin-polarized specular andreev reflections in altermagnets, *Phys. Rev. B* **111**, L100507 (2025).

[83] J. Matsuda, H. Watanabe, and R. Arita, Multiferroic collinear antiferromagnets with hidden altermagnetic spin splitting, *Phys. Rev. Lett.* **134**, 226703 (2025).

[84] Q. N. Meier, A. Carta, C. Ederer, and A. Cano, (Anti-)Altermagnetism from orbital ordering in the ruddlesden-popper chromates  $Sr_{n+1}Cr_nO_{3n+1}$ , *arXiv preprint arXiv:2502.01515* (2025).

[85] S.-D. Guo, Hidden altermagnetism, *Frontiers of Physics* **21**, 025201 (2026).

[86] The states at the  $\Gamma$  point are two-fold degenerate, corresponding to total angular momentum  $\pm 1$ :  $\psi_{\Gamma,\pm} = \frac{1}{\sqrt{2}}(1, 0, 0, \pm i)$  or  $\psi'_{\Gamma,\pm} = \frac{1}{\sqrt{2}}(0, 1, \pm i, 0)$ . The time-reversal symmetry enforces this degeneracy. In contrast, the states at the  $M$  point become non-degenerate—even though they are also superpositions of  $d_{xz}$  and  $d_{yz}$  orbitals with equal weight—because they correspond to total angular momentum 0 or 2 (mod 4):  $\psi_{M,0} = \frac{1}{2}(1, \pm 1) \oplus (1, \pm 1)$  or  $\psi_{M,2} = \frac{1}{2}(1, \pm 1) \oplus (1, \mp 1)$ .

[87] X. Cheng, Y. Gao, and J. P. J. Liu, Realistic tight-binding model for  $V_2Se_2O$ -family altermagnets, *arXiv preprint arXiv:2602.09465* (2026).

[88] M. Smidman, M. Salamon, H. Yuan, and D. Agterberg, Superconductivity and spin-orbit coupling in non-centrosymmetric materials: a review, *Reports on Progress in Physics* **80**, 036501 (2017).

[89] Y. Asano, Numerical method for dc josephson current between d-wave superconductors, *Phys. Rev. B* **63**, 052512 (2001).

[90] K. Sakurai, S. Ikeyama, and Y. Asano, Tunable- $\varphi$  Josephson junction with a quantum anomalous Hall insulator, *Phys. Rev. B* **96**, 224514 (2017).

[91] S.-B. Zhang and B. Trauzettel, Detection of second-order topological superconductors by Josephson junctions, *Phys. Rev. Res.* **2**, 012018 (2020).

[92] To our knowledge, the critical field for the altermagnet-to-ferromagnet transition in  $CsV_2Te_2O$  has not yet been experimentally determined.

[93] H.-P. Sun, S.-B. Zhang, C.-A. Li, and B. Trauzettel, Tunable second harmonic in altermagnetic josephson junctions, *Phys. Rev. B* **111**, 165406 (2025).

[94] B. Lu, K. Maeda, H. Ito, K. Yada, and Y. Tanaka,  $\varphi$  Josephson Junction Induced by Altermagnetism, *Phys. Rev. Lett.* **133**, 226002 (2024).

[95] L. Sharma and M. Thakurathi, Tunable Josephson diode effect in singlet superconductor-altermagnet-triplet superconductor junctions, *Phys. Rev. B* **112**, 104506 (2025).

[96] A. Pal, D. Mondal, T. Nag, and A. Saha, Josephson current signature of floquet majorana and topological accidental zero modes in altermagnet heterostructures, *Phys. Rev. B* **112**, L201408 (2025).

[97] W. Zhao, Y. Fukaya, P. Burset, J. Cayao, Y. Tanaka, and B. Lu, Orientation-dependent transport in junctions formed by d-wave altermagnets and d-wave superconductors, *Phys. Rev. B* **111**, 184515 (2025).

[98] G. Z. X. Yang, Z.-T. Sun, Y.-M. Xie, and K. T. Law, Topological altermagnetic josephson junctions, *arXiv preprint arXiv:2502.20283* (2025).

[99] N. Heinsdorf and M. Franz, Proximityalizing altermagnets with conventional superconductors, *Phys. Rev. B* **113**, L020501 (2026).

[100] R. Peng, J. Yang, L. Hu, W.-L. Ong, P. Ho, C. S. Lau, J. Liu, and Y. S. Ang, All-electrical layer-spintronics in altermagnetic bilayers, *Materials Horizons* **12**, 2197 (2025).

[101] B. Chen, F. Fei, D. Zhang, B. Zhang, W. Liu, S. Zhang, P. Wang, B. Wei, Y. Zhang, Z. Zuo, et al., Intrinsic magnetic topological insulator phases in the sb doped  $MnBi_2Te_4$  bulks and thin flakes, *Nature communications* **10**, 4469 (2019).

[102] S. Zhang, R. Wang, X. Wang, B. Wei, B. Chen, H. Wang, G. Shi, F. Wang, B. Jia, Y. Ouyang, et al., Experimental observation of the gate-controlled reversal of the anomalous hall effect in the intrinsic magnetic topological insulator  $MnBi_2Te_4$  device, *Nano Letters* **20**, 709 (2019).

[103] D. Ovchinnikov, X. Huang, Z. Lin, Z. Fei, J. Cai, T. Song, M. He, Q. Jiang, C. Wang, H. Li, et al., Intertwined topological and magnetic orders in atomically thin chern insulator  $MnBi_2Te_4$ , *Nano letters* **21**, 2544 (2021).

[104] A. Gao, Y.-F. Liu, C. Hu, J.-X. Qiu, C. Tzschaschel, B. Ghosh, S.-C. Ho, D. Bérubé, R. Chen, H. Sun, et al., Layer hall effect in a 2D topological axion antiferromagnet, *Nature* **595**, 521 (2021).

[105] S. Yang, X. Xu, Y. Zhu, R. Niu, C. Xu, Y. Peng, X. Cheng, X. Jia, Y. Huang, X. Xu, J. Lu, and Y. Ye, Odd-even layer-number effect and layer-dependent magnetic phase diagrams in  $MnBi_2Te_4$ , *Phys. Rev. X* **11**, 011003 (2021).

[106] Y.-F. Zhao, L.-J. Zhou, F. Wang, G. Wang, T. Song, D. Ovchinnikov, H. Yi, R. Mei, K. Wang, M. H. Chan, et al., Even-odd layer-dependent anomalous hall effect in topological magnet  $MnBi_2Te_4$  thin films, *Nano letters* **21**, 7691 (2021).

[107] F. Hübner, M. J. Wolf, T. Scherer, D. Wang, D. Beckmann, and H. v. Löhneysen, Observation of andreev bound states at spin-active interfaces, *Phys. Rev. Lett.* **109**, 087004 (2012).

[108] L. Tosi, C. Metzger, M. F. Goffman, C. Urbina, H. Pothier, S. Park, A. L. Yeyati, J. Nygård, and P. Krogstrup, Spin-orbit splitting of andreev states revealed by microwave spectroscopy, *Phys. Rev. X* **9**, 011010 (2019).

[109] G. Wang, L.-S. Liu, Z. Zhu, Y. Zheng, B. Yang, D. Guan, S. Wang, Y. Li, C. Liu, W. Chen, H. Zheng, and J. Jia, Quantum-size effect induced andreev bound states in ultrathin metallic islands proximitized by a superconductor, *Phys. Rev. Lett.* **135**, 076201 (2025).